UC San Diego
UC San Diego Previously Published Works

Title
Nuclear neutrino energy spectra in high temperature astrophysical environments

Permalink
https://escholarship.org/uc/item/9bx6h286

Journal
Physical Review C, 94(5)

ISSN
2469-9985

Authors
Misch, G Wendell
Fuller, George M

Publication Date
2016-11-01

DOI
10.1103/physrevc.94.055808

Peer reviewed

Nuclear neutrino energy spectra in high temperature astrophysical environments

G. Wendell Misch

Department of Physics and Astronomy, Shanghai Jiao Tong University, Shanghai 200240, China
and Collaborative Innovation Center of IFSA (CICIFSA), Shanghai Jiao Tong University, Shanghai 200240, China

George M. Fuller

Department of Physics, University of California, San Diego, La Jolla, California 92093, USA

Astrophysical environments that reach temperatures greater than ∼100 keV can have significant neutrino energy loss via both plasma processes and nuclear weak interactions. We find that nuclear processes likely produce the highest-energy neutrinos. The important weak nuclear interactions include both charged current channels (electron capture and emission and positron capture and emission) and neutral current channels (deexcitation of nuclei via neutrino pair emission). We show that, in order to make a realistic prediction of the nuclear neutrino spectrum, one must take nuclear structure into account; in some cases, the most important transitions may involve excited states, possibly in both parent and daughter nuclei. We find that the standard technique of producing a neutrino energy spectrum by using a single transition with a Q value and matrix element chosen to fit published neutrino production rates and energy losses will not accurately capture important spectral features.

I. INTRODUCTION

In this paper, we calculate energy spectra for neutrinos produced in nuclear weak interaction processes that occur in precollapse massive stars. A key motivation for this work is the possibility of detecting a neutrino signal from a massive star, perhaps even months before collapse [1–4]. Patton & Lunardini (hereafter P&L) [5] have studied the neutrino emissivity physics in this problem and the associated prospects for detection. In this paper, we build on the work of P&L, but we concentrate on the nuclear physics which determines important aspects of the neutrino energy spectra, especially at high neutrino energy. Higher neutrino energies are, of course, key to detection. Our nuclear structure considerations and our shell-model calculations allow us to illuminate features of specific *sd*-shell nuclei which are likely to be key contributors to the high-energy end of the expected neutrino spectrum.

Beginning with core carbon burning, neutrino production dominates the energy loss of massive stars. Depending on the mass of the star and its stage of burning, these neutrinos can be produced through electron-positron pair annihilation, the photoprocess (wherein a photon interacts with an electron and produces a neutrino pair), neutrino pair bremsstrahlung, electron capture, and other processes. In low-mass stars and in massive stars prior to core collapse, the neutrinos stream unimpeded through stellar material, removing entropy from the core and greatly accelerating the evolution of the star [6].

In the final stages before collapse of a massive star, the core is hot and dense, but the entropy is low [7]. The temperature is ∼0.5 MeV, but the electron Fermi energy can be ∼5 MeV, implying very-electron-degenerate conditions [8–20]. The electron degeneracy relatively suppresses neutrino production processes with electrons in the final state, processes with intermediate electron loops, and electron-positron annihilation. At the same time, the high Fermi energy relatively enhances electron capture (Fig. 1), while the high temperature gives a population of excited nuclei that can deexcite by emission

of a neutrino pair (Fig. 2) [21–23]. In many cases, excited nuclei can also more readily decay by electron or positron emission [24], which is always accompanied by an antineutrino or neutrino, respectively (Fig. 3).

High temperatures allow the nuclei to access excited parent states which may have large Q values and large weak interaction matrix elements for charged current transitions. Large Q values imply larger phase-space factors for weak interactions but, against this, Boltzmann population factors for these highly excited initial states can be small. However, ameliorating the effect of small Boltzmann factors is the near-exponential increase in nuclear level densities with increasing excitation energies. In the end, the balance between all these factors must be evaluated on a case-by-case basis for individual nuclei and particular thermodynamic conditions in the star.

This situation has a profound effect on the neutrino spectrum, as energetic electrons can capture onto excited parent nuclei, which might have a *less* excited final state in the daughter nucleus; this results in an unusually-high-energy neutrino.

Furthermore, these excited nuclei may directly produce neutrino pairs. When excited nuclei deexcite, the usual channel is γ-ray emission; however, they may also emit a virtual Z^0 boson that decays into a neutrino antineutrino pair, shown schematically in Fig. 2. In fact, this can be the dominant source of neutrino pairs in a collapsing stellar core [22,23,25–27]. If the nucleus deexcites from a highly excited state, it can produce an energetic neutrino pair of any flavor, and these neutrinos can make a substantial contribution at the high-energy end of the neutrino spectrum.

One final process that we will not discuss but which falls under the general purview of nuclear neutrinos is neutral current inelastic neutrino scattering on nuclei (Fig. 4) [22,28,29]. Scattering does not produce neutrinos, but it can alter the neutrino spectrum. During the event, the nucleus can either gain internal energy from the neutrino in a subelastic
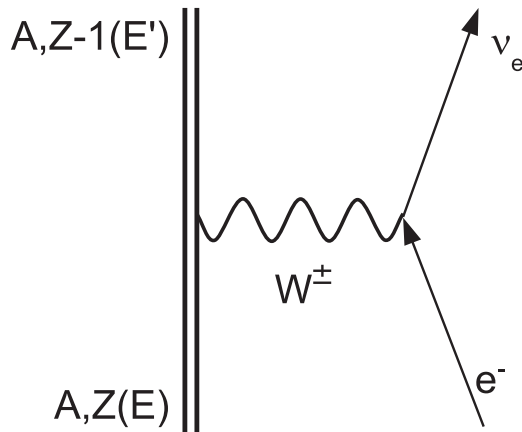
FIG. 1. Electron capture on a nucleus of mass number A, proton number Z, and excitation energy E, producing a nucleus of mass number A, proton number $Z - 1$, and excitation energy E'. The electron and neutrino may be exchanged in this diagram for their antiparticles, yielding a final nucleus with proton number $Z + 1$.

FIG. 3. Electron decay from a nucleus of mass number A, proton number Z, and excitation energy E to a nucleus of mass number A, proton number $Z + 1$, and excitation energy E'. The electron and antineutrino may be exchanged in this diagram for their antiparticles, yielding a final nucleus with proton number $Z - 1$.

scatter, or the nucleus can give up energy to the neutrino in a superelastic scatter. The former will shift the neutrino spectrum down in energy, while the latter will shift it up. Under most circumstances, there will be greater strength for a nuclear "up-transition" [22], meaning a subelastic scatter that lowers neutrino energy. However, in supernova environments, there may be a sufficient population of excited nuclei to shift part of the neutrino spectrum up, lengthening the high-energy tail of the spectrum, with possible implications for detection.

Section II details the calculation of the charged current process neutrino spectra and shows some results of high temperature shell-model calculations. In Sec. III we discuss neutral current nuclear deexcitation neutrino production and spectra, and in Sec. IV, we go over the results and their implications.
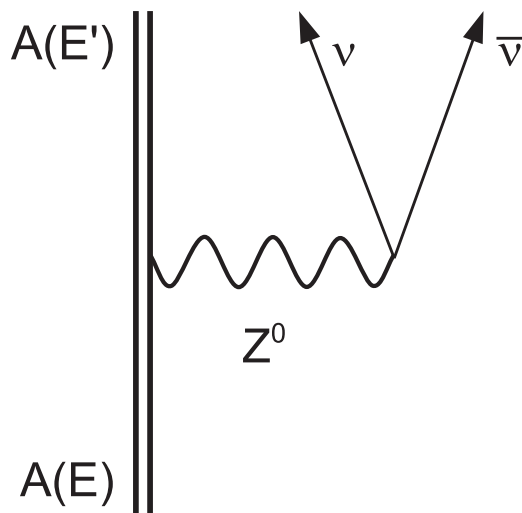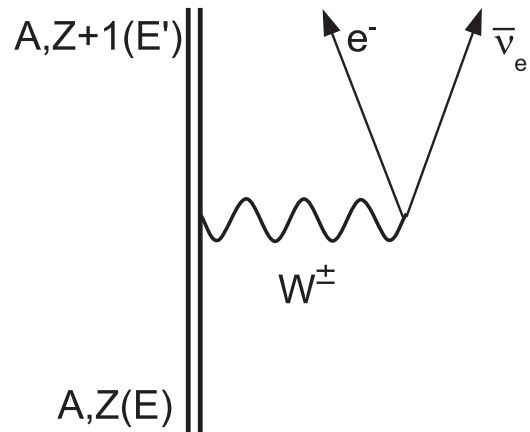
II. CHARGED CURRENT PROCESS NEUTRINOS

Both sd- and pf-shell nuclei will play a role in determining the precollapse neutrino and antineutrino energy spectra and corresponding fluxes. Although we concentrate here on sd-shell nuclei, many of our conclusions on the role of nuclear excited states are also true for pf-shell nuclei. We will speculate on nuclear structure issues for pf-shell nuclei in the Sec. IV discussion.

We carried out nuclear structure computations in the following manner: We used the shell-model code OXBASH [30] to compute energy levels and transition matrix elements of sd-shell nuclei. Our model consisted of a closed ^{16}O core, with the remaining nucleons unrestricted within the sd shell; the $1d_{5/2}$, $2s_{1/2}$, and $1d_{3/2}$ single-particle states comprise the sd shell. We employed the USDB Hamiltonian [31]. Where feasible, we used experimentally determined nuclear state
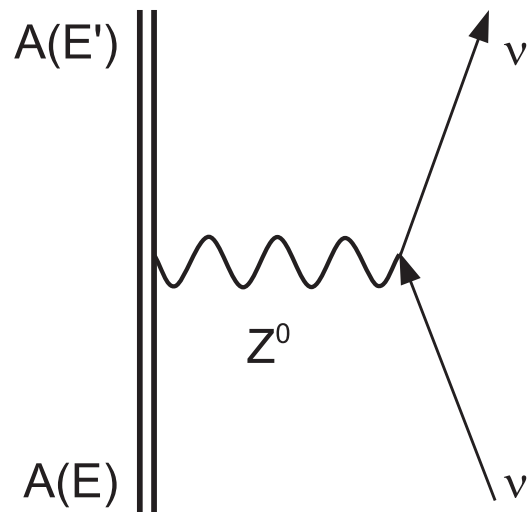

FIG. 2. Neutral current neutrino pair emission from a nucleus of mass number A with initial excitation energy E and final excitation E'.

FIG. 4. Neutral current neutrino scattering from a nucleus of mass number A with initial excitation energy E and final excitation E'.

energies (for most of the nuclei we examined, these were the lowest 10 to 20 positive-parity states) and transition strengths [taken from published log ft values], and we otherwise relied on matrix elements calculated with the code. We quenched the computed (nonexperimental) squared transition matrix elements by a factor of 0.6. We give rates and spectra in s^{-1} baryon^{-1}, and these are calculated as though the *entire stellar core* were comprised of that material; that is, we show the emissivity of, e.g., ^{21}Ne as though the entire stellar core were ^{21}Ne.

We first consider four charged current interactions: electron capture, positron emission, positron capture, and electron emission. The former two produce electron flavored neutrinos via Gamow–Teller and Fermi nuclear transitions—GT$^-$ and F$^-$, respectively—while the latter produce electron flavored antineutrinos via GT$^+$ and F$^+$ transitions.

A. Charged current process calculation

To compute the rates, we follow the prescription of FFNI [32]. The transition rate is given by

$$\lambda_{if} = \ln2 \frac{f_{if}(T,\rho Y_e)}{ft_{if}}, \tag{1}$$

where ft_{if} is the relative half-life of the transition (this factor contains physical constants and the transition matrix elements), and $f_{if}(T,\rho Y_e)$ is the phase-space factor. We take

$$\frac{1}{ft_{if}} = \frac{1}{ft_{if}^{GT}} + \frac{1}{ft_{if}^F} = \frac{B_{if}^{GT\pm}}{10^{3.596}} + \frac{B_{if}^F}{10^{3.791}}, \tag{2}$$

which has units of s^{-1}, where

$$B_{if}^{GT\pm} = \frac{\left|M_{if}^{GT\pm}\right|^2}{2J_i+1} = \frac{\left|\langle f|\sum_k(\overrightarrow{\sigma}\,\tau^\pm)_k|i\rangle\right|^2}{2J_i+1}, \tag{3}$$

$$B_{if}^{F\pm} = \frac{\left|M_{if}^{F\pm}\right|^2}{2J_i+1} = \frac{\left|\langle f|\sum_k(\tau^\pm)_k|i\rangle\right|^2}{2J_i+1}. \tag{4}$$

Here, $\overrightarrow{\sigma}$ is the one-body spin operator, $\tau^\pm$ is the one-body isospin raising (upper sign) and lowering (lower sign) operator, $|i\rangle$ and $|f\rangle$ are the initial and final nuclear states, respectively, and the sums are over nucleons.

The phase-space factor for the decay processes is

$$f_{if} = \int_1^{-q} w^2(-q-w)^2 G(Z,w)[1 - f_{e^\pm}(w)]dw \tag{5}$$

and for the capture processes is

$$f_{if} = \int_{\max(1,q)}^\infty w^2(-q+w)^2 G(Z,w) f_{e^\pm}(w)dw, \tag{6}$$

where w is the electron energy, q is the energy of the transition (daughter energy minus parent energy, including rest mass), G is the Coulomb correction factor (described in detail in FFNI), and $f_{e^\pm}(w)$ is the electron (positron) distribution function; all energies are in units of electron mass m_e. Finally, these individual transition rates are summed over final states and thermally populated initial states.

Here, however, we are interested in neutrino spectra, rather than total rates; we obtain these by changing the phase-space

factor variable of integration from the electron energy to the neutrino energy, then keep only the kernel and do not integrate. After changing variables, we interpret the kernel as the contribution to the transition rate per unit energy of the outgoing neutrino. Since the spectrum is an explicit function of neutrino energy, we want a more convenient unit, so we factor $1/m_e$ out of all energies (yielding a total of four powers of $1/m_e$); this gives the freedom to choose any unit of energy. To more readily compare nuclei, we divide by the mass number A. Now, the units of the spectral density are neutrinos per second per baryon per electron mass; we divide the spectral density by one more power of m_e to allow our choice of energy unit in the denominator. As a consequence, we have

$$S_{if}(E_\nu) = \frac{\ln2}{Am_e^5}\left(\frac{B_{if}^{GT\mp}}{10^{3.596}} + \frac{B_{if}^{F\mp}}{10^{3.791}}\right)E_\nu^2(-Q-E_\nu)^2$$
$$\times G(Z,-Q-E_\nu)[1 - f_{e^\pm}(-Q-E_\nu)]$$
$$\text{neutrinos/(s baryon)} \tag{7}$$

for electron (lower signs) or positron (upper signs) decay and

$$S_{if}(E_\nu) = \frac{\ln2}{Am_e^5}\left(\frac{B_{if}^{GT\pm}}{10^{3.596}} + \frac{B_{if}^{F\pm}}{10^{3.791}}\right)$$
$$\times E_\nu^2(E_\nu+Q)^2 G(Z,E_\nu+Q) f_{e^\pm}(E_\nu+Q)$$
$$\text{neutrinos/(s baryon)} \tag{8}$$

for electron or positron capture, where E_ν is the neutrino energy and Q is the nuclear transition energy. We define Q as the rest mass energy plus final excitation energy of the daughter nucleus minus the rest mass energy plus initial excitation energy of the parent nucleus: $Q = (M_d + E_f) - (M_p + E_i)$. We use MeV for all energies, so the units of the spectrum will be neutrinos per second per baryon per MeV.

We populate the initial states by using the modification of the Brink hypothesis detailed in Ref. [33], considering all states individually up to 12 MeV excitation, and assigning the remaining thermal statistical weight to the average of the next 50 or more higher states. Finally, we sum over initial and final states.

B. Charged current process spectra

In this section, we choose nuclei, temperatures, and densities to facilitate comparison with P&L. That work made the excellent point that charged current processes could be the greatest source of high-energy neutrinos. The authors used the technique of Langanke *et al.* [34] to generate charged current neutrino spectra, whereby a single Q value and transition strength for each nucleus are taken as parameters that are fit to published neutrino-loss and energy-loss rates (such as those of Fuller, Fowler, and Newman [24,32,35,36], Oda *et al.* [37], and Langanke and Martinez–Pinedo [38]). That is, for each nucleus at a particular temperature and electron density (generally expressed as ρY_e), an effective Q value and transition strength are chosen to reproduce the rates published for that nucleus in those conditions. While Langanke *et al.* found that this technique can reasonably produce neutrino (antineutrino) spectra when the typical energy of a captured
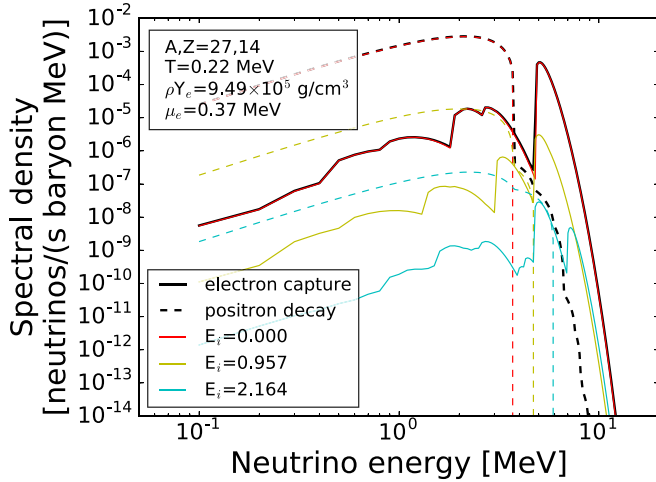
FIG. 5. ^{27}Si charged current process neutrino spectrum. The black lines are totals for the nucleus, and the colored lines correspond to the indicated initial parent states.

FIG. 6. ^{31}S charged current process neutrino spectrum. The black lines are totals for the nucleus, and the colored lines correspond to the indicated initial parent states.

electron (positron) is high enough that nuclear transitions are dominated by the bulk of the transition strength, it may fail when only a few individual transitions produce most of the neutrinos. In contrast, we compute neutrino spectra by the method detailed in the previous section.

Figure 5 shows the neutrino energy spectrum from GT$^-$ and F$^-$ transitions from ^{27}Si to ^{27}Al at a temperature of $\sim$0.22 MeV and $\rho Y_e \sim 9.5 \times 10^5$ g/cm^3. Solid lines are from electron capture, and dotted lines are from positron decay. Black lines are totals for each process, while colored lines are the contributions from selected parent nucleus initial states. Transitions from the ground state dominate the spectrum almost everywhere, although naturally the positron decay spectrum at high neutrino energy comes from excited states. Furthermore, ^{27}Si has a proton excess of exactly 1, while ^{27}Al has a neutron excess of exactly 1, so these two nuclei comprise a mirror system. That is, from a structural perspective, these nuclei are identical up to a relabeling of protons and neutrons. Therefore, each state in ^{27}Si will have a superallowed (Fermi) transition to the corresponding state in ^{27}Al, and in particular, the ground states are therefore connected. Consequently, this transition has a tremendous amount of strength relative to other transitions, and it defines the shape of the spectrum: there is a single large peak from positron decay, and a single large peak from electron capture. The smaller peaks in the electron capture channel arise from transitions to excited states in the daughter nucleus, but outside the narrow valley at $\sim$4 MeV, they are buried under the positron decay peak.

Figure 6 (same line designations as in Fig. 5) shows the neutrino spectrum from GT$^-$ and F$^-$ transitions from ^{31}S to ^{31}P at a temperature of $\sim$0.17 MeV and $\rho Y_e \sim 2.2 \times 10^6$ g/cm^3. As with ^{27}Si and ^{27}Al, these are mirror nuclei, and as in Fig. 5, the ground-state-to-ground-state transitions dominate the spectrum.

Figure 7 (same line designations as in Fig. 5) shows the neutrino spectrum from GT$^-$ and F$^-$ transitions from ^{30}P to ^{30}Si at a temperature of $\sim$0.17 MeV and $\rho Y_e \sim$

2.2×10^6 g/cm^3. This is not a mirror system, so the ground states are not connected by a Fermi transition. Nevertheless, transitions from the ground state of ^{30}P define the neutrino energy spectrum for energies <3 MeV and between 4 and 5 MeV. However, the first-excited state of ^{30}P ($E_i = 0.677$ MeV) is isospin $T = 1$ and spin $J = 0$, so it *does* have a superallowed transition to the ground state of ^{30}Si. The strength of this superallowed transition causes it to dominate the neutrino spectrum from 3 to 3.9 MeV and above 5 MeV neutrino energy. In the narrow band between the high-energy cutoff at 3.9 MeV for positron emission from the first-excited state and the low-energy cutoff at 4.2 MeV for electron capture on the ground state, the third excited state ($E_i = 1.145$ MeV) produces most of the neutrinos. Of course, the population of these excited states depends sensitively on temperature through the Boltzmann factors, so the conclusions may be
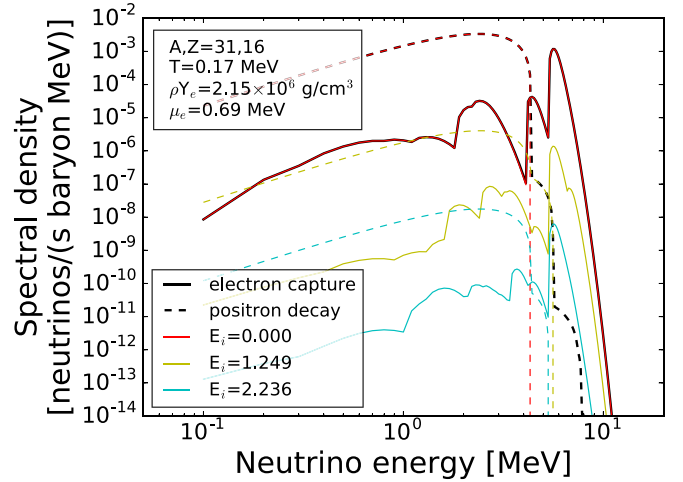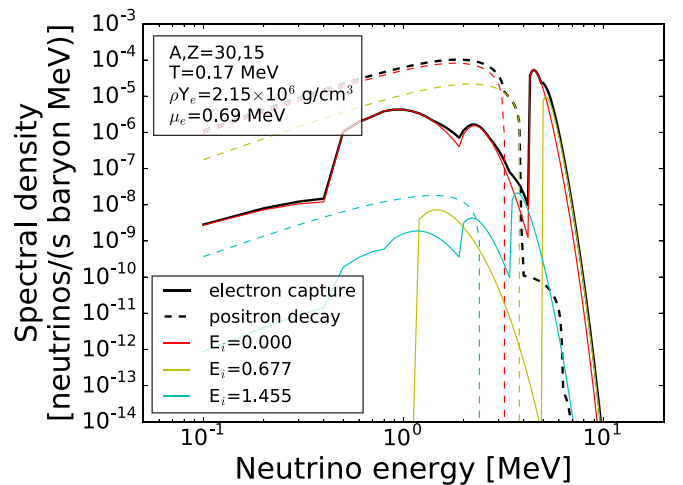

FIG. 7. ^{30}P charged current process neutrino spectrum. The black lines are totals for the nucleus, and the colored lines correspond to the indicated initial parent states.
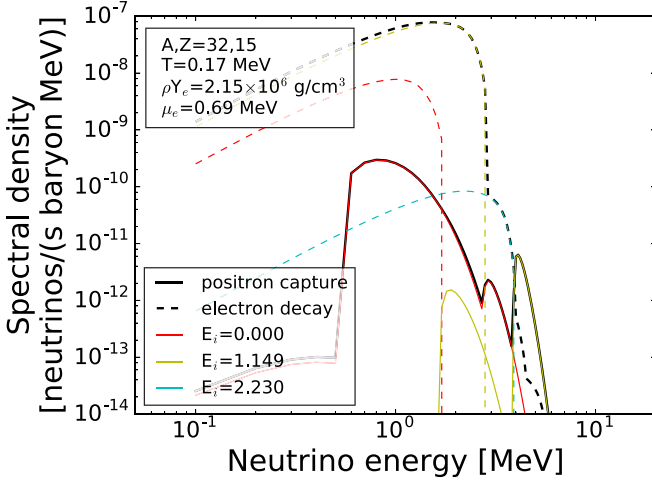
FIG. 8. ^{32}P charged current process antineutrino spectrum. The black lines are totals for the nucleus, and the colored lines correspond to the indicated initial parent states.

FIG. 9. ^{28}Al charged current process neutrino spectrum. The black lines are totals for the nucleus, and the colored lines correspond to the indicated initial parent states.

different at lower temperature or higher temperature than we consider here.

Figure 8 (same line designations as in Fig. 5) shows the antineutrino spectrum from GT$^+$ and F$^+$ transitions from ^{32}P to ^{32}S at a temperature of $\sim$0.17 MeV and $\rho Y_e \sim$ 2.2 × 10^6 g/cm^3. Here, while the ground state does dominate the total positron capture rate, it *nowhere* dominates the spectrum. Instead, transitions from the third excited state ($E_i = 1.15$ MeV) produce most of the spectrum, with the band between 2.7 and 3.9 MeV coming from transitions from the eighth excited state ($E_i = 2.23$ MeV).

The high-energy peak in the positron capture channel on the ground state of ^{32}P arises from transitions to the ground state of ^{32}S. However, this transition has a rather low strength of $B_{GT} = 0.50 \times 10^{-4}$, while the transition to the first-excited state of ^{32}S has a very large strength of $B_{GT} = 0.12$; consequently most of the positron capture neutrinos have low energy. The third excited state ($E_i = 1.15$ MeV), on the other hand, has a high strength transition to the ground state of ^{32}S, with $B_{GT} = 0.074$. The high strength and large phase-space factor overcome the Boltzmann factor relative to ground, resulting in this state being the principle source of electron decay neutrinos and high energy positron capture neutrinos. The ^{32}P $E_i = 2.23$ state also has a fairly high strength transition to ^{32}S ground ($B_{GT} = 0.015$), so electron decay from this state fills the gap between the $E_i = 1.15$ MeV electron decay and positron capture peaks.

Figure 9 (same line designations as in Fig. 5) shows the neutrino spectrum from GT$^-$ and F$^-$ transitions from ^{28}Al to ^{28}Mg at a temperature of $\sim$0.43 MeV and $\rho Y_e \sim$ 1.0 × 10^8 g/cm^3. ^{28}Al is lighter than the typical nucleus in these conditions, but it has close to the correct electron fraction and is therefore an interesting case. The lowest four states of this nucleus have no allowed transitions to the ground state of ^{28}Mg, and as a consequence, they are not significant contributors to the neutrino spectrum at any energy. The fourth, fifth, and eighth excited states ($E_i = 1.37$, 1.62, and 2.20 MeV, respectively) all have allowed transitions to ground and produce most of
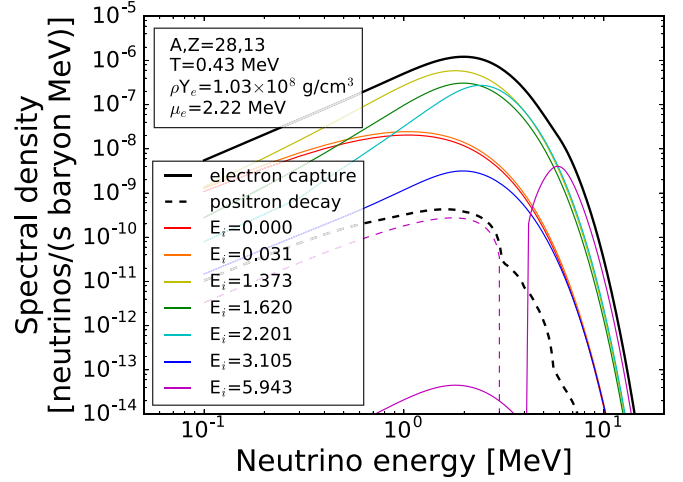
the neutrinos by electron capture. The 15th excited state ($E_i = 3.11$ MeV) has an allowed transition to ^{28}Mg ground, but is hindered by a small thermal population factor and a fairly low transition strength ($B_{GT} = 1.243 \times 10^{-4}$). The first isobaric analog state in ^{28}Al occurs at $E = 5.94$ MeV and is the principle source of positron decay neutrinos and very-high-energy electron capture neutrinos.

III. NEUTRAL CURRENT DEEXCITATION NEUTRINOS

A. Calculation of neutrino pair rates

The deexcitation rate via neutrino pair production from an initial state $|i\rangle$ with energy E_i to a final state $|f\rangle$ with energy E_f is [21]

$$\lambda_{if} \approx \frac{G_F^2 g_A^2}{60\pi^3}(E_i - E_f)^5 B_{if}^{GT3}$$

$$\approx 1.71 \times 10^{-4} s^{-1} \left(\frac{E_i - E_f}{MeV}\right)^5 B_{if}^{GT3}. \qquad (9)$$

G_F is the Fermi constant and g_A is the axial vector coupling constant, and

$$B_{if}^{GT3} = \left| \langle f | \sum_k (\overrightarrow{\sigma} t_z)_k | i \rangle \right|^2 \Big/ (2J_i + 1)$$

is the reduced squared matrix element for the transition; the sum is over nucleons, $\overrightarrow{\sigma}$ is the one-body spin operator, and t_z is the z component of the one-body isospin operator.

The energy-loss rate is, of course, the deexcitation rate times the difference between initial- and final-state energies. Including the thermal population probability of excited states and expressing the transition energy $\Delta E = |E_f - E_i|$ as a ratio to the ambient temperature, the energy-loss rate per nucleus by deexcitation into neutrino pairs from state $|i\rangle$ to
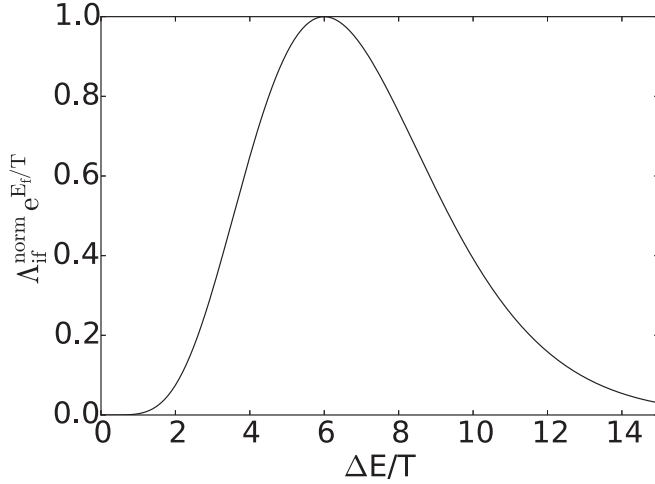
FIG. 10. Normalized energy emission rate in neutrino pairs via deexcitation to a final state with energy E_f for a general nucleus as a function of the ratio of transition energy ΔE to temperature T. This provides a qualitative guide to compare the emission rates of various nuclei at a given temperature.

FIG. 11. Neutrino pair emissivities for a variety of sd-shell nuclei. The odd nuclei stay tightly grouped over the entire range of temperature. At low temperature, ^{28}Si has low emissivity due to a lack of low-lying states.

state $|f\rangle$ is

$$\Lambda_{if} = 1.71 \times 10^{-4} \frac{\text{MeV}}{s} \left(\frac{T}{\text{MeV}}\right)^6 \left(\frac{\Delta E}{T}\right)^6$$
$$\times B_{if}^{GT3} \frac{(2J_i + 1)e^{-(\Delta E + E_f)/T}}{G(T)}, \tag{10}$$

where J_i is the spin of the initial state and $G(T)$ is the nuclear partition function at temperature T.

To guide the search for nuclei that might be important sources of neutrino pairs, we factor out of Eq. (10) the dimensionful factor 1.71×10^{-4} MeV/s, the factor $(T/\text{MeV})^6$, and those parts that depend explicitly on the characteristics of a particular nucleus; to whit, $B_{if}^{GT}(2J_i + 1)/G(T)$, then apply an overall factor of $1/(6^6 e^{-6})$ so that the peak "normalized" emission rate is 1:

$$\Lambda_{if}^{\text{norm}} = \frac{1}{6^6 e^{-6}} \left(\frac{\Delta E}{T}\right)^6 e^{-\Delta E/T} e^{-E_f/T}. \tag{11}$$

From this expression, we see that which nuclei are effective at emitting energy in neutrino pairs depends on the ambient temperature: we seek nuclei with transitions and final states that are low enough in energy that the Boltzmann factor does not overly suppress the population, but balanced against that are the six powers of ΔE that favor higher excitations. Figure 10 shows the normalized emission rate (with the final-state energy dependence factored out) as a function of $\Delta E/T$.

Equation (11) shows that the peak in Fig. 10 lies at $\Delta E/T = 6$. This means that we should look for nuclei that have transitions from excited states to low-lying (preferably ground) states with transition energies near $6T$. The typical range of variation in B_{if}^{GT} for transitions between low-lying states in sd-shell nuclei is about a factor of 10, so we can constrain our search to transition energies between about 3 and 10 times the temperature of the environment of interest.
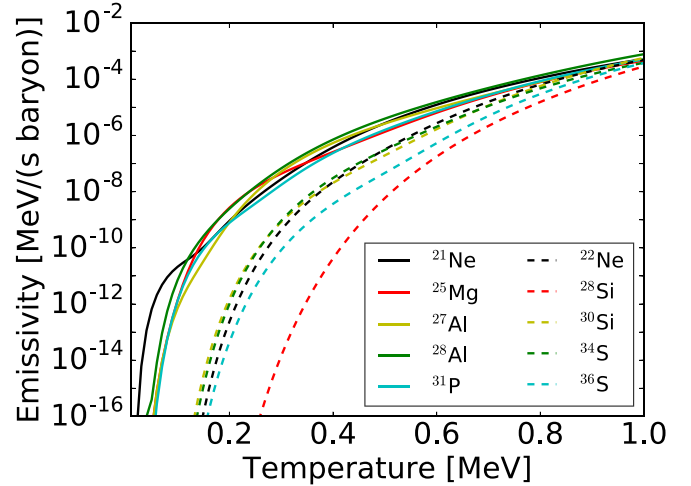
Of course, Eq. (11) applies to individual discrete transitions and does not take the density of states into account. At low energy, states are sparse, so individual transitions tend to dominate the rate at low temperature. As temperature increases, more and more states will fall on the high-energy slope of the peak in Fig. 10, reducing the importance of individual transitions and increasing the most effective energy. As a consequence, at high temperature, the rates can be dominated by the density of states and the overall weak strength energy distribution, and we need not be concerned about the detailed energy-level structure in seeking important nuclei [33].

B. Energy-loss rates

Figure 11 shows the energy-loss rate via neutral current deexcitation of a variety of sd-shell nuclei. The rates are computed by summing Eq. (10) over initial and final states. Following Ref. [33], we considered each state individually up to a cutoff energy, and the remaining statistical weight is carried by a single average high-energy state computed from a sample of states (50 or more) above the cutoff. For each nucleus, we chose a cutoff of 10, 12, or 15 MeV according to how many states in that nucleus we had computed transition matrix elements for. Included in the figure are a selection of odd-even nuclei (nuclei with an even number of protons and an odd number of neutrons or vice versa), the odd-odd nucleus ^{28}Al, the four stable even-even sd-shell nuclei with relatively low-lying ($E < 6$ MeV) $J^\pi = 1^+$ states (which have allowed transitions to ground), and the tightly bound, difficult-to-excite nucleus ^{28}Si.

Over the entire range of temperature, the odd nuclei remain tightly clustered in one group, and the even-even nuclei with low-lying 1^+ states comprise a second group. ^{28}Si falls well below both groups at modest temperatures because it has very few allowed transitions between low-lying states. At high temperature, all of the nuclei converge into a single group, indicating that the behavior at high temperature is independent of the specific nucleus.
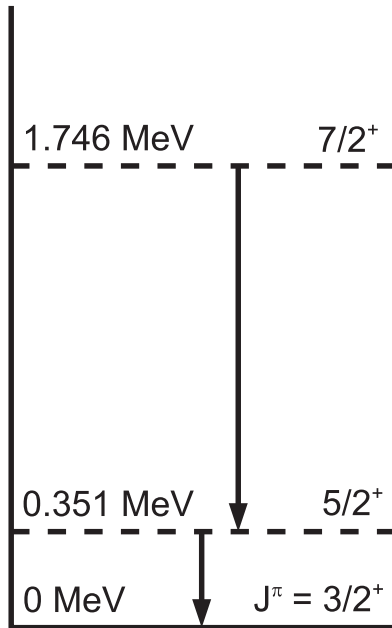
FIG. 12. There are two allowed deexcitations from low-lying excited states in ^{21}Ne. Figure 11 shows that each of these transitions becomes important at different temperatures.

The neutrino and antineutrino emissivity of ^{21}Ne has two prominent ledges as temperature increases. The first occurs at very low temperature (<0.1 MeV), causing ^{21}Ne to dominate the other odd nuclei. We can understand this behavior by examining the low-lying energy-level structure of ^{21}Ne. Figure 12 shows the three lowest-energy states. The first rise is due to the exceptionally low-energy first-excited state, which is substantially lower than the first-excited state of each other nucleus in the figure (except for ^{28}Al, which has a nearly degenerate ground state). Referring to Fig. 10, the transition from the first-excited state to ground reaches peak relative effectiveness at $T \sim 0.06$ MeV, but the next allowed transition does not become effective until $T \sim 0.2$ MeV. This illustrates the importance of individual transitions at low temperatures.

We also compare the energy-loss rates from neutral current deexcitation against the other dominant sources of neutrino emission. Over the temperature and density range relevant to core O-Ne-Mg burning and Si burning, the other two dominant sources of neutrino pairs are electron-positron pair annihilation and the photoprocess [39]. Figure 13 shows the emissivities of ^{27}Al (chosen to represent the odd-nuclei bundle), pair annihilation, and the photoprocess. The rates for the latter two processes are sensitive to density (both decrease with increasing density), so we include the rates for $\rho = 10^7$ (black, upper), 3×10^7 (red, middle), and 10^8 (green, lower) g/cm^3. The bottom panel is a zoom-in on the top panel, emphasizing the temperature range relevant for O-Ne-Mg burning. From these plots, we see that neutral current deexcitation is likely never the dominant source of energy loss via neutrino pairs, but it may nevertheless be a significant contributor.

Electron capture is the final major source of energy loss in highly evolved stellar cores. In Fig. 14, we compare the emissivity of ^{27}Al with the energy-loss rate from electron
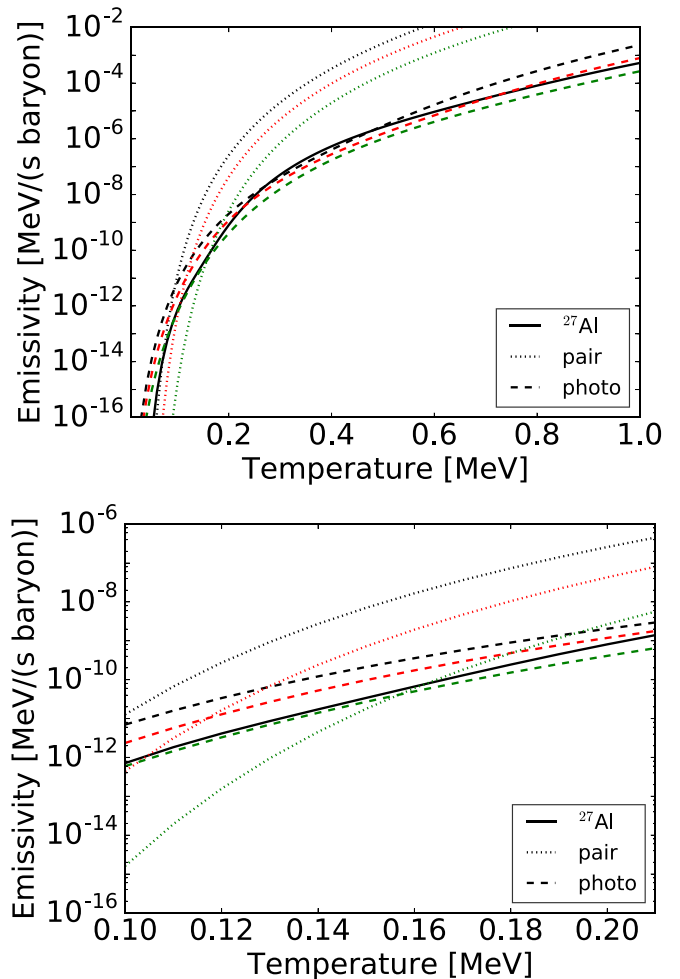

FIG. 13. Energy-loss rates from neutral current deexcitation of ^{27}Al and other major neutrino processes. For electron-positron pair annihilation and the photoprocess, the black (upper) lines are for $\rho = 10^7$ g/cm^3, the red (middle) lines are for 3×10^7 g/cm^3, and the green (lower) lines are for 10^8 g/cm^3. The lower panel emphasizes the temperature range appropriate for core O-Ne-Mg burning.

capture on ^{28}Si. We computed the electron-capture rate by using the prescription of Ref. [33] with a cutoff of 15 MeV. We include $\rho Y_e = 5 \times 10^6$ (black, lower), 5×10^7 (red, middle), and 5×10^8 (green, upper) g/cm^3. The odd-nucleus neutral current rate dominates electron capture on ^{28}Si until very late in silicon burning when the core is near collapse. This comparison is somewhat unfair, however, as ^{28}Si is an even-even nucleus, and odd nuclei tend to have a higher density of states and more allowed transitions. We should be careful, therefore, to not draw broad conclusions from this one comparison and use it only as a guide for further exploration; to accurately compare the two processes, we must know the abundances and relative production rates of many nuclei.

C. Neutral current spectra

Although neutral current deexcitation of nuclei is probably not a major source of energy loss in O-Ne-Mg burning and Si burning, the energies of the pairs can be much greater than the typically thermal energies of pairs produced by other
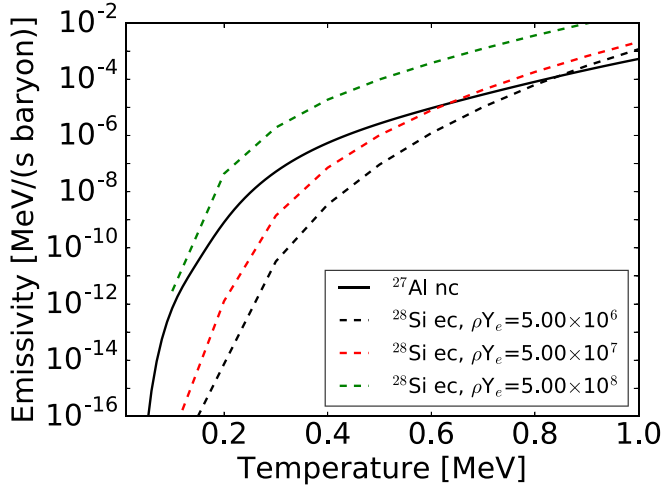
FIG. 14. Energy-loss rates from neutral current deexcitation of ^{27}Al and electron capture on ^{28}Si. The product of density and electron fraction ρY_e is in g/cm^3.

processes. The spectral density of neutrinos from deexcitation from the initial nuclear state $|i\rangle$ to the final state $|f\rangle$ is computed similarly to the spectrum from charged current processes. In this case, the kernel of the phase-space integral that yielded Eq. (9) is simply $E_\nu^2(-Q - E_\nu)^2$, giving a spectral density of

$$S_{if}(E_\nu) = 5.134 \times 10^{-3} \frac{B_{if}^{GT3}}{A^{-1}} \left(\frac{E_\nu}{MeV} \right)^2 \left(\frac{-Q - E_\nu}{MeV} \right)^2$$

$$\text{neutrinos/(s baryon MeV).} \quad (12)$$

We sum Eq. (12) over final states and thermally populated initial states as before, producing a complete spectrum for the nucleus.

Figure 15 shows the neutrino spectra for ^{27}Al (top panel) and ^{28}Si (bottom panel) at a selection of temperatures relevant to late stellar evolution; by symmetry, the antineutrino spectra are identical. We calculated these spectra by using a further modification of the cutoff method detailed above, with the difference being that selections of states above the cutoff are grouped into energy bins which we average over; this avoids overpopulating the very-high-energy tails of the spectra.

Remarkably, above 10 MeV, the spectra of both nuclei are nearly identical. That such different nuclei produce similar high-energy neutrino spectra, coupled with the convergence of emissivities at high temperature in Fig. 11, suggests that all sd-shell nuclei will produce similar results. We included in Fig. 15 very high temperatures relevant at the onset of and during core collapse. An interesting feature of deexcitation pairs is that their rates and spectra are *entirely independent* of the electron density, so that in a highly evolved precollapse and early collapse core, this might be a dominant source of high-energy neutrinos.

IV. DISCUSSION

Detecting neutrinos from highly evolved precollapse stars could give key insights into stellar evolution. This is an exciting prospect.
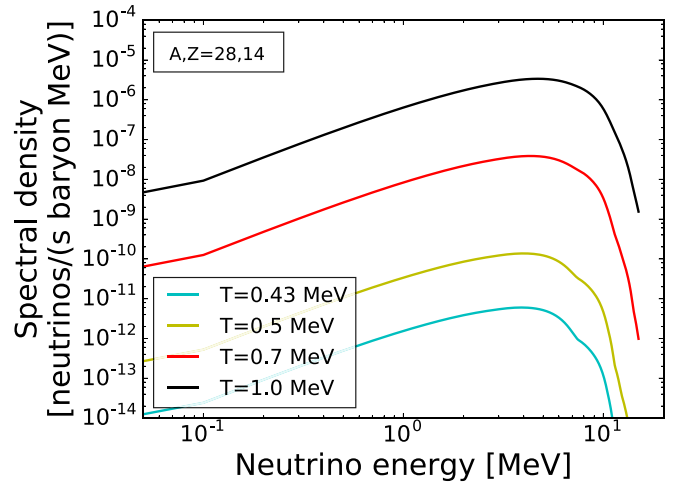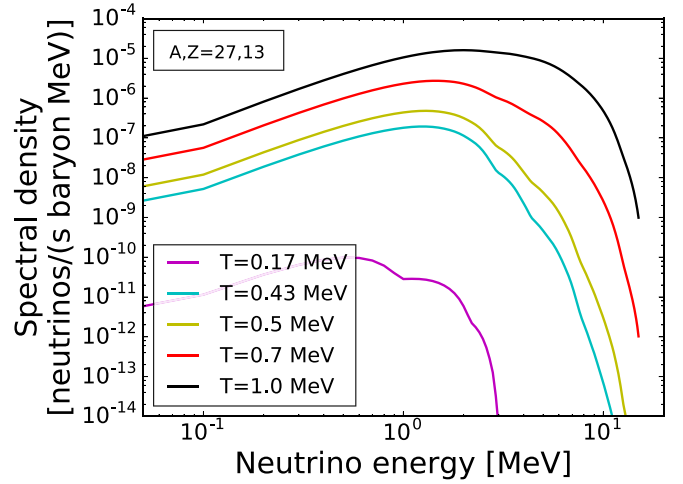

FIG. 15. ^{27}Al (top) and ^{28}Si (bottom) neutral current neutrino spectra. Antineutrino spectra are identical. Notably, the spectra above 10 MeV are similar.

P&L astutely point out the importance of nuclear neutrinos in understanding late stellar neutrino spectra, and we build on that by examining the effects of nuclear structure. To that end, we draw specific attention to ^{32}P, shown in Fig. 8 of this work and Fig. 3 of P&L [5]. In P&L Fig. 3, there is a small bump in the antineutrino spectrum at ~ 4 MeV that the authors say is due positron capture on ^{32}P. At that point in P&L's simulation, the mass fraction of ^{32}P is $\sim 10^{-4}$ (personal communication). By using the mass fraction and the density of the core, we convert the P&L y axis and find that the height of the P&L ^{32}P 4 MeV antineutrino peak is $\sim 8.5 \times 10^{-10}$ neutrinos/(s baryon MeV). This corresponds roughly with the height of the ~ 1 MeV positron capture neutrino peak in our Fig. 8. By design, the single-Q-value technique will give the correct total neutrino output with the correct average energy but, in this case, the energetics of the positron capture neutrinos are incorrect. In this particular case, the published rates are dominated by electron emission from the first-excited parent state, but most captures occur between the parent ground state and the first-excited state of the daughter, pushing the positron capture neutrino energy down; this results in erroneous conclusions from the single Q-value method. Similarly, the single Q-value

method fails to capture the significant contribution of 3–4 MeV antineutrinos from the $E_i = 2.23$ MeV state.

Finally, comparing Fig. 15 in this work with the final plot in Fig. 4 of P&L indicates that, in late silicon burning, neutral current deexcitation may be a leading source of antineutrinos with energies greater than 10 MeV. This is contradicted by the ^{28}Al spectrum in this work's Fig. 9, however, so we must be circumspect in drawing conclusions. Nevertheless, it is clear that the production rates of >10 MeV neutrinos increase dramatically with temperature (due to the exponential dependence of the Boltzmann factor for excited states), and these rates are entirely unaffected by density and the associated baggage (such as electron blocking). This implies that in this neutrino energy range, the effectiveness of this process relative to charged current processes is highly sensitive to the ambient temperature, and no solid conclusions can be drawn until realistic nuclear neutrino spectra are included in a simulation. At higher temperatures—approaching the onset of collapse—neutral current deexcitation may be the dominant source of >10 MeV neutrinos.

During core collapse, the electron chemical potential μ_e climbs as density increases, with the consequence that the average energy of a captured electron is very high. When μ_e reaches the energy of the Gamow–Teller resonance of a typical nucleus, the capture rate takes off, producing neutrinos prodigiously. Following precisely the method of FFN, we computed electron capture and positron decay neutrino spectra for ^{56}Fe. Using the FFN prescription, ^{56}Fe has a GT resonance at ~ 8 MeV. Figure 16 (same line designations as in Fig. 5) shows the spectra for two points leading up to and during collapse. The upper panel has $\mu_e = 2.22$ MeV (less than the resonance), and the lower panel has $\mu_e = 9.66$ MeV (greater than the resonance). The increase in temperature is not large, but bringing μ_e above the resonance energy increases the peak in the spectrum by more than four orders of magnitude.

Figure 17 shows the ^{56}Fe electron neutrino energy spectra computed by using the FFN prescription at several points during collapse. The solid lines are for electron capture, the dotted lines are for positron decay, and the colors correspond to different temperature and density conditions. The results of Figs. 16 and 17 are qualitative (strength is unquenched, δ-function resonance, etc.) but indicate that, at high μ_e, the distribution of the bulk of the strength dominates the effects of precise structure.

Our technique of modifying the Brink hypothesis (by averaging high-energy states) does not, strictly speaking, obey the thermal detailed balance described in Fischer *et al.* Eq. (10) [27].

$$S^{GT3}(T, \Delta E) = e^{\Delta E/T} S^{GT3}(T, -\Delta E). \qquad (13)$$

Here, S^{GT3} is the neutral current thermal strength function [defined analogously to the charged current thermal strength function in Eq. (15)], ΔE is the nuclear transition energy, and T is the temperature. With modification, this equation also applies to charged current interactions.

$$G_j(T)S_{jk}^{\pm}(T, Q) = e^{(Q - \Delta m)/T} G_k(T)S_{kj}^{\mp}(T, -Q). \qquad (14)$$

The plus (minus) signs in the superscripts refer to isospin raising (lowering) transitions, Q is the change in total nuclear
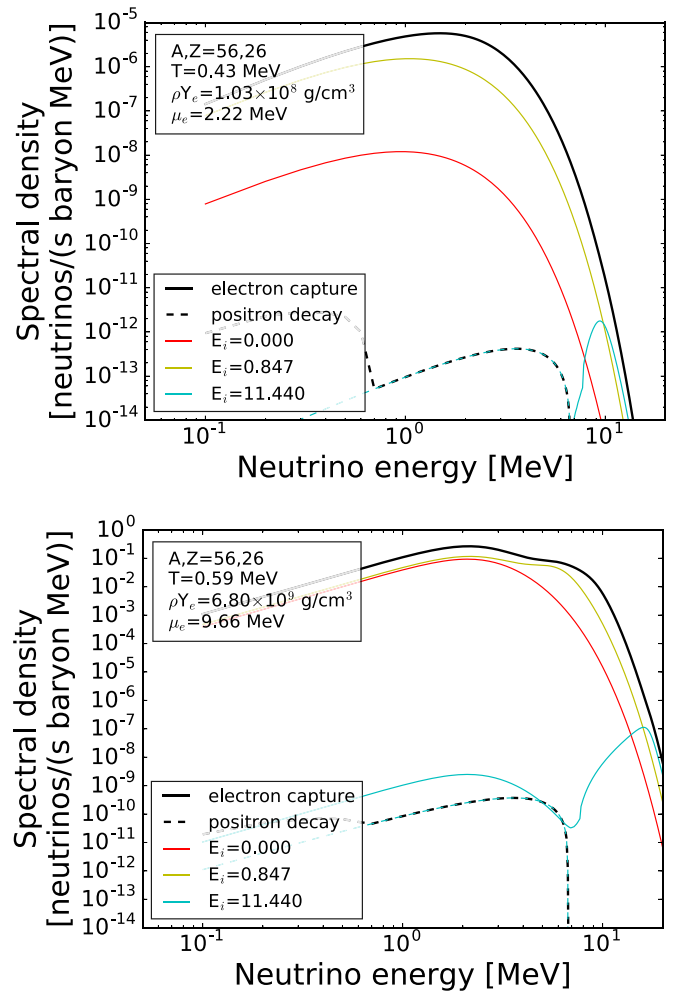

FIG. 16. ^{56}Fe charged current process neutrino spectra computed from the FFN prescription. The $E_i = 11.44$ MeV line corresponds to the isobaric analog of the ^{56}Mn ground state. In the upper panel, the electron chemical potential is less than the Gamow–Teller resonance energy, while in the lower panel, it is greater than the GT resonance energy. Because of this, the peak in the lower panel is more than four orders of magnitude greater, despite the comparatively small increase in temperature.

energy, Δm is the rest mass energy of nucleus k minus the mass of nucleus j, $G_{j(k)}$ is the partition function of nucleus j (k), and $S_{jk}^{\pm}$ is the thermal strength function for transitions from nucleus j to nucleus k, defined as

$$S_{jk}^{\pm}(T, Q) = \frac{1}{G_j(T)} \int_0^{\infty} dE (2J_j + 1) \rho_j(E, J_j)$$
$$\times e^{-E/T} B_{jk}^{\pm}(E, Q), \qquad (15)$$

where J_j is the spin of the state in nucleus j with excitation energy E, $\rho_j(E, J_j)$ is the density of states in nucleus j, and $B_{jk}^{\pm}(E, Q)$ is the strength (GT or Fermi) for the state with energy E to make a transition to nucleus k with transition energy Q.

In our approach, the strengths from states with initial nuclear excitation energy above the chosen cutoff are treated
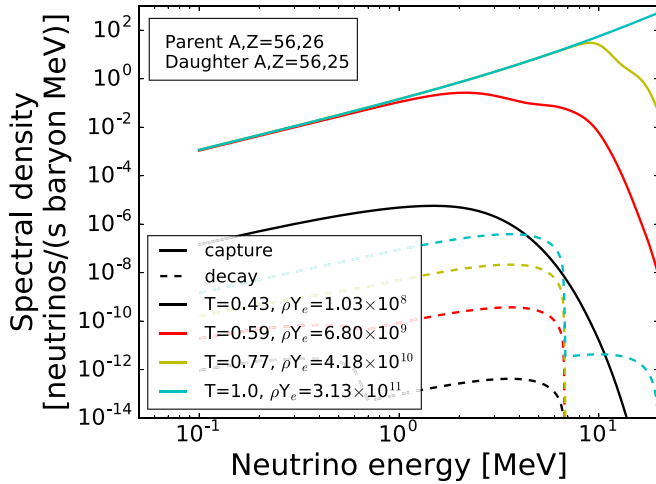
FIG. 17. ^{56}Fe charged current process neutrino spectra computed from the FFN prescription at various points during collapse. The enormous jump in neutrino production between the lowest two temperatures is due to the chemical potential in the higher temperature point being greater than the Gamow–Teller resonance energy.
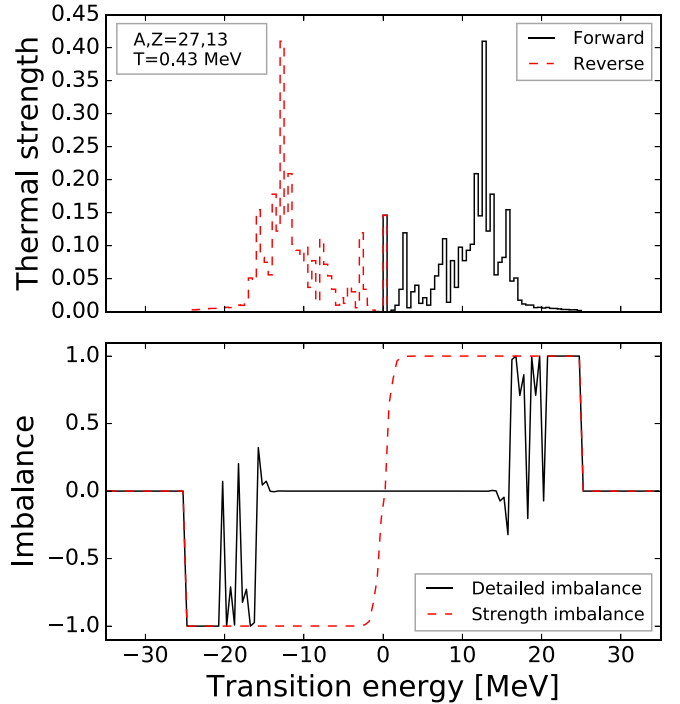

FIG. 18. ^{27}Al thermal strength at temperature $T = 0.43$ MeV. The upper panel shows the thermal strengths in the left (forward) and right (reverse) sides of Eq. (17); these are *only* the thermal strengths and do *not* include the exponential factors. The lower panel shows the imbalance between the right- and left-hand sides of Eq. (17) (detailed imbalance, solid line) and the imbalance of the thermal strengths (dashed line).

in an average sense, whereas strengths from lower initial energy to states with final nuclear energy above the cutoff are treated individually. This difference in treatment means that transitions involving initial or final states above the cutoff do not obey Eqs. (13) and (14); this is in contrast to other approaches, such as the thermal quasiparticle random-phase approximation [40]. However, we expect this violation to be unimportant for a few reasons; the right-hand side is, of course, summed over spins.

First, at the temperatures and densities considered here, nuclear states above 12 MeV do not contribute much to the charged current neutrinos; the typical electron and positron energies are low enough that captures to final nuclear states above 12 MeV are very rare, and initial states above 12 MeV are not heavily populated. Second, because neutrinos stream freely out, the core material is not in weak equilibrium, so the forward and reverse reactions will not proceed at the same rate. In other words, although the nuclear matrix elements for the forward and reverse reactions must be identical by the principle of detailed balance, the phase-space factors are very different because the neutrinos are not in thermal and chemical equilibrium. This is especially true in the case of the neutral current channel, where the inverse of neutrino pair emission is pair annihilation on a nucleus; there are not enough neutrinos present for this reaction to occur at a meaningful rate.

A deeper analysis provides further evidence that our technique does not violate detailed balance in an important way. We define the imbalance I between two positive quantities A and B as

$$I(A, B) = \frac{A - B}{A + B}. \tag{16}$$

When A and B are equal, the imbalance is zero, and when one or the other is much larger, the imbalance is near -1 or 1.

Rewriting Eq. (13) as

$$e^{-\Delta E/2T} S^{GT3}(T, \Delta E) = e^{\Delta E/2T} S^{GT3}(T, -\Delta E) \tag{17}$$

puts the forward (left-hand side) and reverse (right-hand side) reactions on equal footing. The imbalance in Eq. (17) is then computed by assigning the right-hand side to the quantity A and the left-hand side to B in Eq. (16). This gives us a measure of thermal detailed balance: where the quantities are balanced, the imbalance is zero.

Figure 18 gives a picture of how our approach violates thermal detailed balance in the neutral current channel. We choose ^{27}Al as a representative case because of its high density of states and many allowed neutral current transitions, but other nuclei behave similarly. The upper panels show the thermal strength distribution for the forward and reverse reactions, where "forward" refers to the thermal strength on the left-hand side of Eq. (17) and "reverse" refers to the strength on the right-hand side (including the negative transition energy in the argument). In the case of neutral current transitions, these strengths are simply mirror images of one another, but we show both for the sake of later discussion. The lower panel shows the imbalance of the forward and reverse thermal strength distributions (dashed line) and the imbalance of left- and right-hand sides of Eq. (17), which we term "detailed imbalance."

Our technique produces regions of transition energy where detailed balance is not satisfied. However, wherever the detailed imbalance is large, so is the imbalance in the thermal

strength, indicating that either the forward or reverse reaction had comparatively little strength in that region anyway. Even more telling is that the imbalance is only large far out on the tail of one or the other of the thermal strengths, where that strength would naturally be exceedingly small, and therefore contribute little to the rates and spectra. Everywhere else, detailed balance holds. Consequently, we are confident that our technique for calculating rates and spectra produces reliable results for the nuclei in the precollapse conditions considered here.

Given the obvious importance of nuclear contributions to neutrinos with detectable energies, we will move forward in generating tabulated nuclear neutrino energy spectra in the same vein as the neutrino production and energy-loss rates of earlier works.

[1] A. Odrzywolek, M. Misiaszek, and M. Kutschera, Astropart. Phys. **21**, 303 (2004).

[2] A. Odrzywolek, M. Misiaszek, and M. Kutschera, Acta Phys. Pol. B **35**, 1981 (2004).

[3] A. Odrzywolek and A. Heger, Acta Phys. Pol. B **41**, 1611 (2010).

[4] K. Asakura *et al.* (KamLAND Collaboration), Astrophys. J. Lett. **818**, 91 (2016).

[5] K. M. Patton and C. Lunardini, arXiv:1511.02820.

[6] S. E. Woosley, A. Heger, and T. A. Weaver, Rev. Mod. Phys. **74**, 1015 (2002).

[7] H. A. Bethe, G. E. Brown, J. Applegate, and J. M. Lattimer, Nucl. Phys. A **324**, 487 (1979).

[8] W. D. Arnett, Astrophys. J. **218**, 815 (1977).

[9] R. Bowers and J. R. Wilson, Astrophys. J. **263**, 366 (1982).

[10] H. A. Bethe and J. R. Wilson, Astrophys. J. **295**, 14 (1985).

[11] J. M. Blondin, A. Mezzacappa, and C. DeMarino, Astrophys. J. **584**, 971 (2003).

[12] J. M. Blondin and A. Mezzacappa, Nature (London) **445**, 58 (2007).

[13] L. Scheck, H.-T. Janka, T. Foglizzo, and K. Kifonidis, Astron. Astrophys. **477**, 931 (2008).

[14] T. D. Brandt, A. Burrows, C. D. Ott, and E. Livne, Astrophys. J. **728**, 8 (2011).

[15] A. Arcones, H.-T. Janka, and L. Scheck, Astron. Astrophys. **467**, 1227 (2007).

[16] M. Liebendörfer, T. Fischer, C. Fröhlich, W. R. Hix, K. Langanke, G. Martinez-Pinedo, A. Mezzacappa, S. Scheidegger, F.-K. Thielemann, and S. C. Whitehouse, New Astron. Rev. **52**, 373 (2008).

[17] M. Liebendörfer, T. Fischer, M. Hempel, A. Mezzacappa, G. Pagliara, I. Sagert, J. Schaffner-Bielich, S. Scheidegger, F.-K. Thielemann, and S. C. Whitehouse, Nucl. Phys. A **827**, 573c (2009).

[18] N. J. Hammer, H.-T. Janka, and E. Müller, Astrophys. J. **714**, 1371 (2010).

[19] W. R. Hix, E. J. Lentz, M. Baird, O. E. B. Messer, A. Mezzacappa, C.-T. Lee, S. W. Bruenn, J. M. Blondin, and P. Marronetti, Nucl. Phys. A **834**, 602c (2010).

[20] A. Burrows, J. C. Dolence, and J. W. Murphy, Astrophys. J. **759**, 5 (2012).

[21] J. N. Bahcall, S. B. Treiman, and A. Zee, Phys. Lett. B **52**, 275 (1974).

[22] G. M. Fuller and B. S. Meyer, Astrophys. J. **376**, 701 (1991).

[23] G. W. Misch, B. A. Brown, and G. M. Fuller, Phys. Rev. C **88**, 015807 (2013).

[24] G. M. Fuller, W. A. Fowler, and M. J. Newman, Astrophys. J. **252**, 715 (1982).

[25] S. S. Gershtein, V. N. Folomeshkin, M. I. Khlopov, and R. A. Eramzhian, Zh. Eksp. Teor. Fiz. **69**, 1121 (1975).

[26] E. W. Kolb and T. J. Mazurek, Astrophys. J. **234**, 1085 (1979).

[27] T. Fischer, K. Langanke, and G. Martínez-Pinedo, Phys. Rev. C **88**, 065804 (2013).

[28] S. E. Woosley and W. C. Haxton, Nature (London) **334**, 45 (1988).

[29] S. E. Woosley, D. H. Hartmann, R. D. Hoffman, and W. C. Haxton, Astrophys. J. **356**, 272 (1990).

[30] B. A. Brown, A. Etchegoyen, N. S. Godwin, W. D. M. Rae, W. Richter, W. E. Ormand, E. K. Warburton, J. S. Winfield, L. Zhao, and C. H. Zimmerman, MSU-NSCL Report No. 1289 (2004).

[31] B. A. Brown and W. A. Richter, Phys. Rev. C **74**, 034315 (2006).

[32] G. M. Fuller, W. A. Fowler, and M. J. Newman, Astrophys. J., Suppl. Ser. **42**, 447 (1980).

[33] G. W. Misch, G. M. Fuller, and B. A. Brown, Phys. Rev. C **90**, 065808 (2014).

[34] K. Langanke, G. Martínez-Pinedo, and J. M. Sampaio, Phys. Rev. C **64**, 055801 (2001).

[35] G. M. Fuller, W. A. Fowler, and M. J. Newman, Astrophys. J., Suppl. Ser. **48**, 279 (1982).

[36] G. M. Fuller, W. A. Fowler, and M. J. Newman, Astrophys. J. **293**, 1 (1985).

[37] T. Oda, M. Hino, K. Muto, M. Takahara, and K. Sato, At. Data Nucl. Data Tables **56**, 231 (1994).

[38] K. Langanke and G. Martínez-Pinedo, At. Data Nucl. Data Tables **79**, 1 (2001).

[39] N. Itoh, H. Hayashi, A. Nishikawa, and Y. Kohyama, Astrophys. J., Suppl. Ser. **102**, 411 (1996).

[40] A. A. Dzhioev, A. I. Vdovin, and J. Wambach, Phys. Rev. C **92**, 045804 (2015).